



## ZnFe-layered double hydroxide nanostructures prepared from natural iron ore precursors with the hydrothermal method and the photocatalytic degradation of Rhodamine B

Atit Wannawek<sup>a</sup>, Pongthep Jansanthea<sup>b,\*</sup>, Weerasak Chomkitichai<sup>b</sup>, Jiraporn Ketwaraporn<sup>b</sup>, Kannikar Jumpa<sup>b</sup>, Chanaporn Ruangrit<sup>b</sup>, Intranee Thangoen<sup>b</sup>, Kanitha Rattanasatian<sup>b</sup>, Chaowarit Wansao<sup>c</sup>, Aimon Wanaek<sup>c</sup>, Pusit Pookmanee<sup>d</sup>

<sup>a</sup>Department of Science, Rajamangala University of Technology Lanna Lampang, Lampang, Thailand, email: atit\_wannawek@rmutl.ac.th

<sup>b</sup>Program in Chemistry, Faculty of Science and Technology, Uttaradit Rajabhat University, Uttaradit 53000, Thailand,

Tel.: +66-84-5045373; emails: pongthep.jan@uru.ac.th (P. Jansanthea), weerasak.cho@uru.ac.th (W. Chomkitichai),

j.ketwaraporn@hotmail.com (J. Ketwaraporn), mo\_kannikar@hotmail.com (K. Jumpa), u60031520106@uru.ac.th (C. Ruangrit),

Intranee7223@gmail.com (I. Thangoen), Kainthafar@gmail.com (K. Rattanasatian)

<sup>c</sup>Program in Physics, Uttaradit Rajabhat University, Uttaradit, Thailand, emails: wansaw@gmail.com (C. Wansao),

aimon.wan@uru.ac.th (A. Wanaek)

<sup>d</sup>Program in Applied Chemistry, Maejo University, Chiang Mai, Thailand, email: pusit@mju.ac.th

Received 31 October 2022; Accepted 14 March 2023

---

### ABSTRACT

This paper investigates the use of low-cost natural iron ore in the preparation of binary metal layered double hydroxide (ZnFe-LDH) nanostructures via a hydrothermal process. In particular, the photocatalytic degradation of Rhodamine B under UV light irradiation is utilized. Natural iron ore is used to prepare the iron(III) precursors ( $\text{Fe}^{3+}$ ) necessary for building the ZnFe-LDH nanostructures. Preparation is done at 80°C–100°C for 36 h and does not involve a calcination process. The physicochemical characterizations of the prepared samples are carried out via X-ray diffraction, Fourier-transform infrared spectroscopy, energy-dispersive X-ray spectroscopy, scanning electron microscopy, UV-Vis diffuse reflectance spectroscopy, and photoluminescence. After confirming the existence of the ZnFe-LDH nanostructures via their functional groups and elemental compositions, it is noted that they have high crystallinity and small crystal sizes. The morphologies of the ZnFe-LDH nanostructures are irregular, with small particles agglomerated on their surfaces. While good optical properties are enhanced as the preparation temperature is increased, the results show that crystallinity, crystal size, particle uniformity, and narrow bandgap energy play important roles in the subsequent photocatalytic reactions. The optimum conditions for the photodegradation of 10 ppm Rhodamine B solution are reached with 1.00 g/L of ZnFe-LDH nanostructures prepared using the hydrothermal method at 100°C for 36 h. At maximum efficiency, the photodegradation process can be completed at a rate constant of 0.2060  $\text{min}^{-1}$  in 20 min and an  $E_{\text{EO}}$  of 44.74 kWh/ $\text{m}^3$  with the addition of a 0.9% v/v  $\text{H}_2\text{O}_2$  electron acceptor. Photocatalyst efficiency decreases by just 12.5% across five test cycles.

*Keywords:* ZnFe-LDH; Iron ore; Hydrothermal; Photocatalytic; Energy consumption

---

\* Corresponding author.

## 1. Introduction

In recent decades, industrial advancement and increasing urbanization have resulted in various kinds of environmental pollution around the world, especially water pollution [1]. Organic pollutants are known as the main contaminant type of wastewater. Dyes are the most important pollutants that can be produced in the textile, paint, paper, and plastic industries. A significant source of water contamination comes from using synthetic dyes in numerous sectors. Rhodamine B (RhB) is a basic dye belonging to a group of heterocyclic organic compounds with a wide range of industrial applications. Human exposure can result in burning eyes, damage to the respiratory system, vomiting, cyanosis, rapid heartbeat, tissue necrosis, nausea, and diarrhea [2]. In addition, it causes serious environmental problems due to its high toxicity and accumulation in the environment. Therefore, water purification is gaining widespread scientific interest [3,4]. There are several methods used to remove impurities, such as adsorption, oxidative processes, electrochemical degradation, and photocatalytic reactions. Among many other techniques, the photocatalytic process has attracted a lot of attention. The advantages of photocatalytic treatment include its flexibility to respond to environmental variables, the use of oxygen that has been dissolved in aqueous media for operations, and the complete mineralization of organic contaminants into more benign by-products [5]. In this type of photocatalytic reaction, a photocatalyst is irradiated, and electron ( $e^-$ )/hole ( $h^+$ ) pairs are photogenerated on its surface. These pairs form highly reactive species, such as hydroxyl radicals ( $OH^\bullet$ ), superoxide anion radicals ( $O_2^{\bullet-}$ ), and  $H_2O_2$ , which induce redox reactions to degrade organic pollutants [6]. Recently, photocatalysts of various semiconductors have been developed for enhanced photocatalysis. Therefore, researchers are focused on the development of new and efficient semiconductors. Various types of photocatalysts are constantly being researched and developed. But there is still a fundamental need to deliver an efficient and useful catalyst through a cheap, easy, and environmentally-friendly route. Most importantly, a semiconductor must be cost-effective to meet future energy and environmental demands [7,8].

One of the new materials for environmental treatment applications is layered double hydroxides (LDHs) because LDHs are good adsorbents and also have good photocatalytic properties such as a high specific surface area, easy preparation, low cost, and high stability [9]. LDHs are well known as a class of two-dimensional anionic clays composed of positively charged metal hydroxide sheets and charge compensating interlayer anions. These are generally expressed by the classical formula  $[M^{2+}_{(1-x)}M^{3+}_x(OH)_2]^{x+}(A^{n-})_{x/n} \cdot mH_2O$ , where  $M^{2+}$  represents a divalent cation such as  $Mg^{2+}$ ,  $Zn^{2+}$ ,  $Ni^{2+}$ ,  $Ca^{2+}$ , etc., and  $M^{3+}$  represents a trivalent cation, for example,  $Al^{3+}$ ,  $Fe^{3+}$ ,  $Cr^{3+}$ ,  $Mn^{3+}$ , etc.  $A^{n-}$  stands for the interlayer anions of valence  $n$  ( $CO_3^{2-}$ ,  $SO_4^{2-}$ ,  $NO_3^-$ ,  $Cl^-$ , or  $PO_4^{3-}$ , etc.).  $x$  is the molar ratio of  $M^{3+}/(M^{2+}+M^{3+})$ , and  $m$  is the number of water molecules present in the layered structure [10–12]. LDHs are the popular inorganic hosts for the formation of nanocomposite or nanolayered composite materials, and they have received much attention in the past decades due to their vast applicability in areas such as

nanotechnology, biotechnology, adsorption, catalysis, and photocatalysis [13].

Natural iron ore predominantly contains hematite ( $\alpha-Fe_2O_3$ ), a rich and inexpensive mineral that can be prepared as a photocatalytic material [14].  $Fe_2O_3$  is the cheapest, most stable, and most environmentally-friendly semiconductor material, but it has limitations for its photocatalytic activity, such as a high electron–hole recombination rate, weak conductivity and low diffusion length of the hole, and low conductivity [15]. The photocatalytic properties of  $Fe_2O_3$  can also be enhanced with composites with other metals such as zinc [16]. For efficiency and cost-effectiveness, ZnFe-LDH can be synthesized at a lower heat consumption than oxide for iron/zinc composites [17]. As mentioned above, ZnFe-LDH is attractive as a photocatalyst material due to its low cationic toxicity and compatibility of  $Zn^{2+}$  and  $Fe^{3+}$  [18]. An example of the application of ZnFe-LDH as a photocatalyst for environmental remediation, such as the degradation of aqueous methyl violet (MV) and malachite green (MG) [19], the removal of *Microcystis aeruginosa* (algae) [20], and the oxidation of ofloxacin (antibiotics) [21], etc. A binary metal ZnFe-LDH has been successfully prepared by numerous methods and precursors [22–24]. These precursors can be good candidates for the synthesis of ZnFe-LDH nanostructures. The preparation and benefits of nanocomposites or nanostructures have been reported several times for their outstanding applications and can act as a suitable photocatalytic agent. They can potentially exhibit significant advantages in environmental applications, such as wastewater purification using nanomaterials and/or nanocomposites [25,26].

Herein, we report on the novel natural iron ore precursors for facile simple one-step hydrothermal preparation of ZnFe-LDH nanostructures. The goal of this research was to increase the value of natural low-cost material in a simple and effective process that could be used as a guideline for large-scale production. This research involved preparing ZnFe-LDH nanostructures from natural iron ore precursors with the chemical precipitation-hydrothermal method and testing for the photocatalytic degradation of RhB from an aqueous solution. Their structural and optical properties have been studied by X-ray diffraction (XRD), Fourier-transform infrared spectroscopy (FT-IR), energy-dispersive X-ray spectroscopy (EDXS), scanning electron microscopy (SEM), UV-Vis diffuse reflectance spectroscopy (UV-DRS), and photoluminescence spectroscopy (PL) techniques. The effects of the photocatalyst preparation temperature, the electron acceptor concentration for the reaction efficiency, the energy consumption of the photodegradation process, and the photocatalyst reusability were studied.

## 2. Materials and methods

### 2.1. Materials

The natural iron ore in this experiment was obtained from natural resources in the Namphee sub-district, Thongsaenkhan District, Uttaradit Province, Thailand. The other chemicals were analytical grade reagents, including hydrochloric acid (HCl, 35.4%, Loba Chemie, India), hydrogen peroxide ( $H_2O_2$ , 30% v/v, Merck, Germany), zinc acetate dihydrate ( $Zn(CH_3COO)_2 \cdot 2H_2O$ , 99.5%, Loba Chemie,

India), sodium hydroxide (NaOH, 98%, Loba Chemie, India), Rhodamine B ( $C_{28}H_{31}ClN_2O_3$ , 95%, Loba Chemie, India), isopropanol ( $C_3H_8O$ , 99.5%, Loba Chemie, India), ethylene diamine tetra-acetic acid ( $C_{10}H_{16}N_2O_8$ , 99.4%, Loba Chemie, India), and L-ascorbic acid ( $C_6H_8O_6$ , 99.5%, Loba Chemie, India). All of the solutions were prepared with deionized (DI) water.

## 2.2. Preparation of natural iron ore

Natural iron ore is characterized by small granules of magnetite ( $Fe_3O_4$ ) mixed with reddish-brown hematite powder. In this research, natural iron ore was sifted through a 200-mesh sieve to collect only the powdered hematite for use in the subsequent preparation of the  $Fe^{3+}$  solution. 20 g of sifted iron ore powder were mixed with 100 mL of 6 M HCl and stirred for 30 min, followed by hydrothermal treatment at 100°C for 10 h under autogenous pressure. After cooling, filtration was used to separate the suspension and retain only parts of the solution. After that, 10 mL of concentrated  $H_2O_2$  was added into a solution for the oxidation of  $Fe^{2+}$  to  $Fe^{3+}$  ions. The concentration of  $Fe^{3+}$  ions was calculated using the titration method.

## 2.3. Preparation and characterization of ZnFe-LDH photocatalysts

The ZnFe-LDH nanostructures were prepared with the 0.05 M zinc acetate and 0.05 M  $Fe^{3+}$  solutions described in the previous section. These two solutions were slowly mixed together. Then 6 M of NaOH solution was added dropwise to the mixture under continuous and vigorous stirring until the pH of the reaction was alkaline (pH~10.0) and precipitation was complete. Once the solution was homogeneous, the suspensions were transferred to a sealed Teflon autoclave and kept at 80°C–100°C for 36 h, then cooled to room temperature. The precipitates were separated from the reaction medium via filtration and then thoroughly washed with deionized water until neutral pHs were reached. Finally, the powders were dried at 60°C for 24 h for further use. The pure  $Fe_2O_3$  and pure ZnO, separate precipitates were obtained via the same process and treated at 100°C for 36 h.

The final samples were characterized via X-ray powder diffraction (Bruker/D2 Phaser, Germany) with  $CuK\alpha$  radiation ( $\lambda = 1.5418 \text{ \AA}$ ) while scanning from 10° to 80° at a rate of 0.02°/s. Fourier transform infrared spectroscopy (Perkin Elmer Spectrum RX I, UK), energy-dispersive X-ray spectroscopy (Oxford Instruments, Ultim Max 40, UK), scanning electron microscopy (TESCAN VEGA3, Czechia), UV-Vis diffuse reflectance spectroscopy (Shimadzu UV-3101PC, Japan), and photoluminescence spectroscopy (Avantes AvaSpec-2048TEC, Netherlands) were also utilized.

## 2.4. Photocatalytic studies

The photocatalytic set-up consisted of 50 mL test tube glass reactors, an initial RhB concentration of 10 ppm, 0.050 g of photocatalyst, and two six-watt UV-C tube lamps (Sylvania, G6W, Japan), as shown in Fig. 1. The UV lamps were utilized due to their high effectiveness and low energy consumption. In each test, chemical adsorption-desorption equilibrium was achieved through stirring continuously for 30 min, then letting the system sit for 30 min in a

black-walled box without external illumination. Next, 3 mL samples were collected for evaluation at approximately 0, 5, 10, 15, 20, 30, and 40 min. Finally, the samples were filtered through a 0.22  $\mu\text{m}$  syringe filter (MS® MCE Syringe filter, Membrane Solution, USA). These tests were then used to create a guideline for developing future treatment systems.

The absorbance of the RhB solution was measured with a UV-Vis spectrophotometer (T90+, PG Instruments, UK). More details can be found in our previous report [27,28]. The degradation efficiency (DE (%)) was calculated using the following equation [21]:

$$DE(\%) = \left[ 1 - \left( \frac{A_t}{A_0} \right) \right] \times 100 \quad (1)$$

where  $A_0$  and  $A_t$  are the initial absorbance of the RhB and its absorbance after the photocatalytic process, respectively. The pseudo-first-order kinetic model was used to evaluate the photocatalytic degradation of the RhB under UV light irradiation as well as the corresponding reaction rates ( $k$ ), which could be calculated from the following equation [21]:

$$\ln \left( \frac{A_0}{A_t} \right) = Kt \quad (2)$$

where  $K$  is the reaction rate constant ( $\text{min}^{-1}$ ), and  $A_0$  and  $A_t$  are the initial and final absorbances of the RhB solution at 0 min and  $t$  min, respectively.

### 2.4.1. Active species trapping test

To find out the reactive species in the synthesized ZnFe-LDH photocatalysts. The photocatalytic degradation of RhB over the ZnFe-LDH photocatalysts under UV light irradiation enabled the active species trapping tests. The experiment was monitored after the addition of 4 mM solutions of isopropanol (IPA), ethylenediaminetetraacetic acid (EDTA), and L-ascorbic acid (AA) as the scavengers for  $OH^\bullet$ ,  $h^+$ , and  $O_2^{\bullet-}$ , respectively.

### 2.4.2. Effect of the electron acceptor concentration

With the effect of the electron acceptor concentration,  $H_2O_2$  was used as an electron acceptor to evaluate the

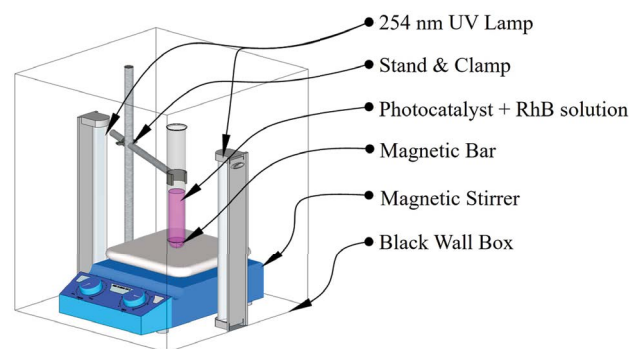


Fig. 1. Illustration of the photocatalytic experimental set-up.

photocatalytic activity of the prepared samples. Different concentrations of  $\text{H}_2\text{O}_2$ , approximately 0.0% v/v, 0.3% v/v, 0.6% v/v, and 0.9% v/v, were studied with the most efficient photocatalyst.

#### 2.4.3. Reusability test

The reusability of each photocatalyst was investigated by repeatedly degrading the fresh RhB solution (10 ppm) across five test cycles. After each typical photocatalytic experiment, the photocatalyst was separated out via centrifugation and then washed with 10 mL of ethanol for 1 h under magnetic agitation. Then the recycled photocatalyst was reused under the same conditions.

### 3. Results and discussion

#### 3.1. Characterization of ZnFe-LDH photocatalysts

##### 3.1.1. XRD analysis

The X-ray diffraction patterns of the samples prepared with the hydrothermal method are shown in Fig. 2. As illustrated in Fig. 2a, all of the XRD patterns show major peaks at  $2\theta = 24.1^\circ, 33.2^\circ, 35.7^\circ, 40.8^\circ, 49.5^\circ, 54.1^\circ, 62.5^\circ, 64.1^\circ$  and  $72.6^\circ$ , which correspond to the (012), (104), (110), (113), (024), (116), (214), (300), and (119) peaks of rhombohedral  $\alpha\text{-Fe}_2\text{O}_3$ , in accordance with the Joint Committee on Powder Diffraction Standards (JCPDS) file No. 00-033-0664

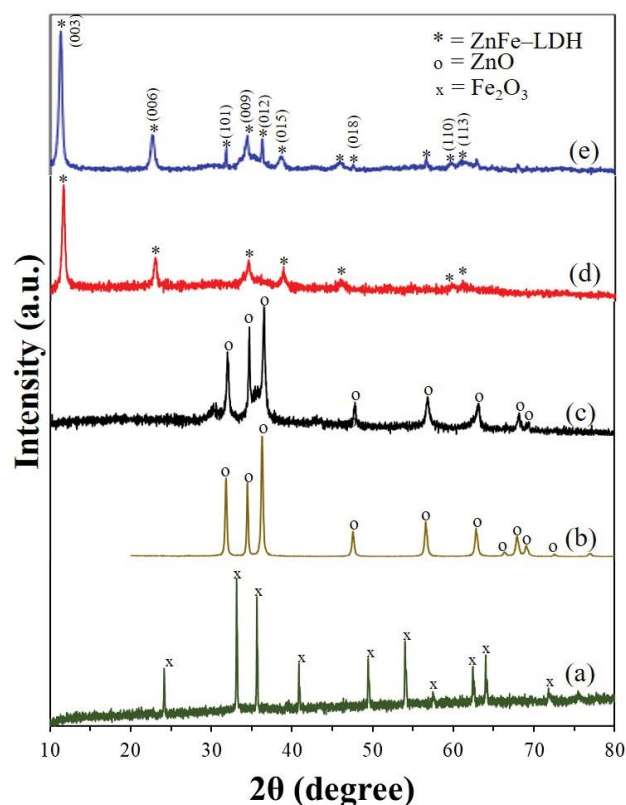


Fig. 2. X-ray diffraction patterns of (a)  $\text{Fe}_2\text{O}_3$ , (b) ZnO, and ZnFe-LDH samples prepared with the hydrothermal method at (c)  $80^\circ\text{C}$ , (d)  $90^\circ\text{C}$ , and (e)  $100^\circ\text{C}$ .

[29]. Fig. 2b shows the main characteristic peaks at the  $2\theta$  values of  $31.9^\circ, 34.6^\circ, 36.4^\circ, 47.7^\circ, 56.8^\circ, 63.0^\circ, 66.5^\circ, 68.1^\circ, 69.2^\circ,$  and  $72.8^\circ$ , corresponding to the (100), (002), (101), (102), (110), (103), (200), (112), (201), and (204) diffraction planes of hexagonal ZnO, respectively (JCPDS file No. 01-079-0205). All of the reflections of the sample prepared at  $80^\circ\text{C}$  (Fig. 2c) corresponded to crystalline ZnO. The peaks representing the other phases were not yet apparent in this sample. For the samples prepared at  $90^\circ\text{C}$  (Fig. 2d), the reflection peaks around  $11^\circ, 24^\circ, 35^\circ, 39^\circ, 47^\circ, 59^\circ,$  and  $61^\circ$  corresponded to the reflections of planes hkl (003), (006), (009), (015), (012), (110), and (113) of Zn-Fe layered double hydroxide (ZnFe-LDH), which were the typical characteristic peaks of hydrotalcite [20]. At higher preparation temperatures (Fig. 2e), the signal intensity of the characteristic peaks of the ZnFe-LDH also increased. As well, the main peaks of the prepared ZnFe-LDH occur at the  $2\theta$  angles of  $11^\circ$  and  $24^\circ$  (Fig. 2d and 1e). The peak found at  $32^\circ$  can be attributed to the ZnO phase, which forms when there are a large number of  $\text{Zn}(\text{OH})_2$  crystallization centers in the brucite-like layer [20]. The prepared samples at  $90^\circ\text{C}$ – $100^\circ\text{C}$  were observed to have a successful formation for the ZnFe-LDH crystal phase. The signal intensity of the (003) and (006) peaks (LDH peaks) was increased with the increase of the preparation temperature. A higher crystallinity of the (003) and (006) peaks was observed, which indicated the presence of a well-ordered layered structure [30]. The average crystallite size was calculated by employing Scherrer's formula [31]:

$$D = \frac{0.9\lambda}{\beta \cos \theta} \quad (3)$$

where  $D$ ,  $\lambda$ ,  $\beta$ , and  $\theta$  represent the crystallite size, the wavelength of the X-ray used, the full width at half maximum (FWHM, in radians), and the Bragg diffraction angle, respectively. The average crystallite sizes of the prepared ZnFe-LDH obtained at different preparation temperatures were 20.54 and 17.15 nm for ZnFe-LDH prepared at  $90^\circ\text{C}$  and  $100^\circ\text{C}$ , respectively. The smaller crystallite size of the particles implies a larger photocatalyst surface area. The ZnFe-LDH prepared at  $80^\circ\text{C}$  did not show major LDH peaks, so the crystal size could not be calculated. The small crystal sizes in the ZnFe-LDH enable the rapid transfer of electrons from the valence band to the conduction band. They also inhibit electron-hole recombination, leading to enhanced photocatalytic activity [32]. Crystallite size is one of the important factors that have a vital role in photocatalytic activity [19].

##### 3.1.2. FT-IR analysis

The FT-IR spectra of samples prepared at  $80^\circ\text{C}$ – $100^\circ\text{C}$  for 36 h in the range of  $400$ – $4,000 \text{ cm}^{-1}$  at room temperature are shown in Fig. 3. The absorption bands below  $1,000 \text{ cm}^{-1}$  were the M–OH and M–O vibration modes of ZnFe-LDH [33,34]. A broad strong absorption band centred at  $3,420 \text{ cm}^{-1}$  was attributed to the stretching vibrations of the surface and interlayer water molecules and hydroxyl groups in the LDH layers, which were found at lower frequencies in the LDH compared with the O–H stretching vibration in free water at

3,600  $\text{cm}^{-1}$  [31,35]. The bands at 1,634  $\text{cm}^{-1}$  could be attributed to the bending vibration of the water molecules adsorbed between them [36]. Other peaks, such as the peak band at approximately 2,850–2,950  $\text{cm}^{-1}$  of the C–H stretch vibration [37], were likely acetate ions from the precursors. The Cl<sup>-</sup> vibration at 830  $\text{cm}^{-1}$  might have been from the precursors of the natural iron ore preparation process [19,20]. The FT-IR patterns of all three samples prepared at 80°C–100°C

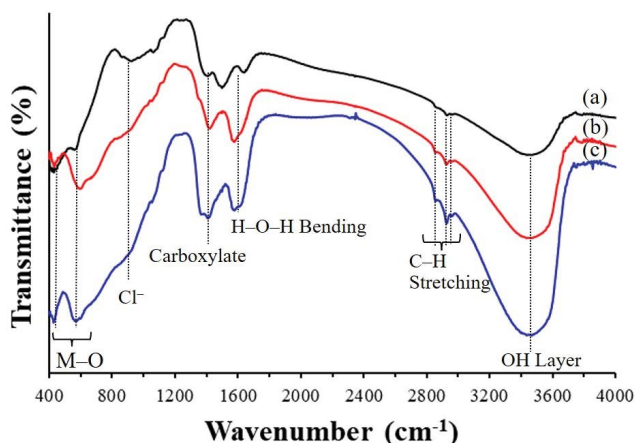


Fig. 3. Fourier-transform infrared spectra of ZnFe-LDH nanostructures prepared with the hydrothermal method at (a) 80°C, (b) 90°C, and (c) 100°C.

were very similar and the peak intensity was increased by the preparation temperature. Based on these similar peaks, it was more probable that the one prepared at 80°C was ZnFe-LDH.

### 3.1.3. EDXS analysis

EDXS analysis was also employed to ascertain the chemical composition of the selected area on the surface of the raw materials and ZnFe-LDH nanostructures, as shown in Fig. 4. For the inset of the EDXS spectra, we report the chemical composition detected with the relative percentage in weight (wt.%). The main element composition of the natural iron ore consisted of Si, Fe, and Al (Fig. 4a). Other elements, such as Au and C, were generated by the analytical equipment and process. After the iron ore preparation process for Si removal, the main remaining element was Fe and a small amount of Al was left (Fig. 4b). When the ZnFe-LDH was prepared at various hydrothermal reaction temperatures, lattice oxygen and Cl anions were correctly intercalated between the metallic layers (Fig. 4d–f). The percentage of Fe by weight increased as the reaction temperature increased in the range 80°C to 100°C, and the  $M^{2+}/M^{3+}$  molar ratio decreased from 3.15 to 2.12 in that same range. According to the literature, if the molar ratio is too high, then a low substitution rate for  $M^{3+}$  in the  $M^{2+}(\text{OH})_2$  layers induces the formation of LDH with strongly reducing porosity [38]. Hence, a low  $M^{2+}/M^{3+}$  ratio is preferred for LDH synthesis. In previous works, the Zn/Fe ratio has

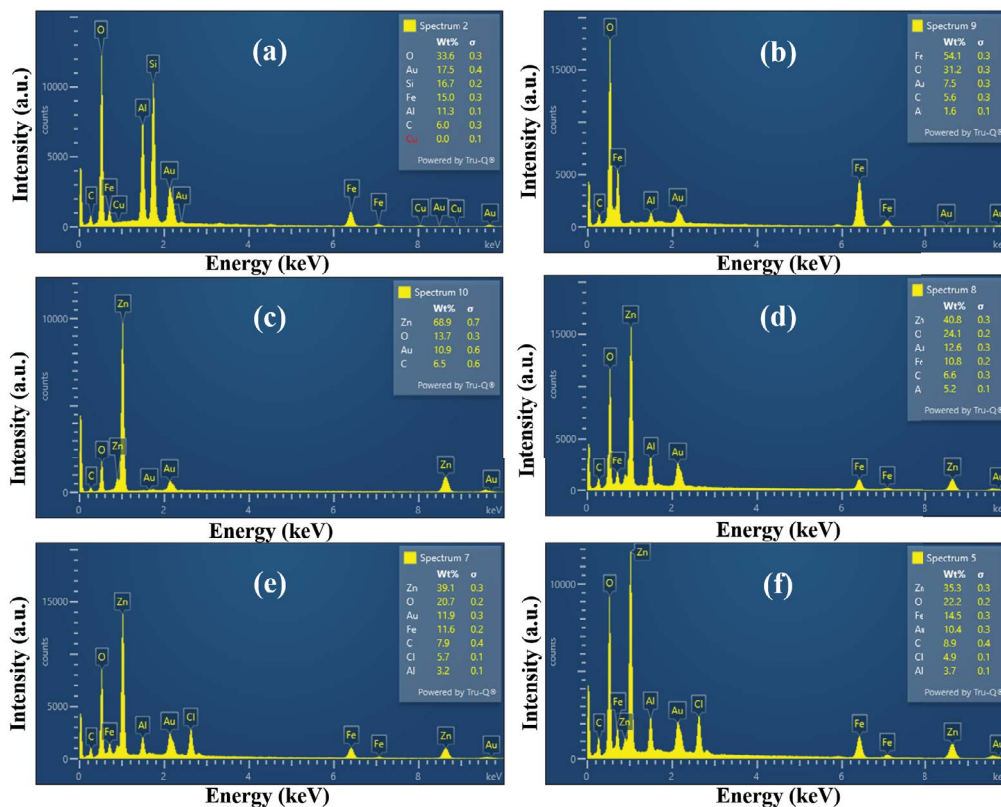


Fig. 4. Energy-dispersive X-ray spectra of (a) iron ore, (b) Fe<sub>2</sub>O<sub>3</sub>, (c) ZnO, and ZnFe-LDH nanostructures prepared with the hydrothermal method at (d) 80°C, (e) 90°C, and (f) 100°C.

ranged from 1 to 3 [35,38,39]. The ZnFe-LDH nanostructures showed the presence of elemental chlorine that matched the FT-IR results and were consistent with the ZnFe-Cl-LDH catalyst from a previous report by Motlagh et al. [21]. These results confirmed the successful formation of ZnFe-LDH particles. The ZnFe-LDH samples were denoted by the preparation temperature as ZnFe-LDH80, ZnFe-LDH90, and ZnFe-LDH100 for the ZnFe-LDH samples prepared with the hydrothermal method at 80°C, 90°C, and 100°C, respectively.

### 3.1.4. SEM analysis

The particle size and the surface morphology of the samples were evaluated using SEM microscopy. Fig. 5 shows the SEM micrograph of the prepared samples with 10,000× magnification. The morphology of the natural iron ore (Fig. 5a) was a rectangular lump with small particles scattered on the surface and particle sizes of approximately 30 μm × 30 μm. The morphology of the pure Fe<sub>2</sub>O<sub>3</sub> as shown in Fig. 5b, was a uniformly distributed spherical particle with a diameter of approximately 0.5–1.5 μm. The pure ZnO Fig. 5c had uniform small rod particles with sizes of approximately 1.0–2.0 μm. The morphology of the ZnFe-LDH nanostructures prepared from natural iron ore (Fig. 5d–f) showed that all three samples were irregular in shape, with tiny particles clumping on the surface [1,21]. At higher preparation temperatures, the surface-bound particle size was also larger. These results confirmed the successful formation of ZnFe-LDH particles.

### 3.1.5. Optical analyses

The efficiency of a photocatalyst involves light absorption and light-induced electrons and holes, which are the key factors controlling a photocatalytic reaction. The electronic excitation of a photocatalyst after the absorption of energy from the light source can be applied to calculate the optical band gap energy ( $E_g$ ). The light absorption properties of the prepared samples were detected with UV-Vis DRS, as illustrated in Fig. 6. In Fig. 6a, it can be seen that the absorbance of the prepared samples overlapped between the UV light region and the visible light region. A crystalline semiconductor's optical absorption near the band edge follows the equation [19,20,40]:

$$(\alpha h\nu)^{1/n} = K(h\nu - E_g) \quad (4)$$

where index  $n$  determines the type of transition, that is, it takes the values 1/2, 2, 3/2, or 3 for directly allowed, indirectly allowed, forbidden direct, and forbidden indirect transitions, respectively. Hence, for direct transitions of ZnFe-LDH nanoparticles,  $n$  is 1/2 [40]. Fig. 6d–f exhibits the bandgap energies of the ZnFe-LDH nanostructures, which were found to be 2.08, 2.00, and 1.95 eV for ZnFe-LDH80, ZnFe-LDH90, and ZnFe-LDH100, respectively. These bandgaps are narrower than those for ZnFe-LDH prepared via chemical co-precipitation without a hydrothermal step [21]. The bandgap energies were decreased when the preparation temperature was increased. This implied that the

photo-absorption of ZnFe-LDH100 was strongest, which resulted in the highest photocatalytic activity [19].

Fig. 7 shows the PL spectra of the ZnFe-LDH nanostructures, which were analysed to confirm the optical properties of the samples. The PL spectra of all the ZnFe-LDH nanostructures activated at 590 nm showed sharp radiation peaks at 665 nm, with the peak intensity increasing with the increasing preparation temperature. This revealed more separation capacity for the  $e^-/h^+$  pairs and the formation of  $OH^\bullet$  [21]. However, the hydroxide groups present on the surface of the ZnFe-LDH nanostructures contributed to the reduction of the  $e^-/h^+$  recombination, resulting in better photocatalytic activity. Furthermore, the  $e^-/h^+$  recombination could be reduced by adding an electron acceptor in the photocatalytic process [41]. The photoluminescence studies confirmed an increase in the emission intensities with the increasing preparation temperature due to the reduction of the bandgap energy.

### 3.2. Photocatalytic activity

The photocatalytic behaviour and the pseudo-first-order kinetic plot of the prepared ZnFe-LDH nanostructures were evaluated using the degradation of the RhB in an aqueous solution under UV light irradiation, as shown in Fig. 8. The photocatalytic efficiency and the kinetic rate constant values of the samples are shown in Table 1. The highest efficiency for the photocatalytic degradation of RhB was that for the ZnFe-LDH100 catalyst with a degradation efficiency of 68.53%, and a kinetic rate constant of 0.0348 min<sup>-1</sup> in 40 min. Based on this result, the photocatalytic efficiency was increased by increasing the preparation temperature. This was because increasing the preparation temperature resulted in better photocatalytic properties such as higher crystallinity, reduced crystal size, and reduced bandgap energy. The preparation of LDH using the hydrothermal method could be easier for tuning structures and morphologies [7]. Radical chemistry plays an important role in photocatalysis. The quantity and the chemical nature of the radicals generated in a particular photocatalytic reaction are highly dependent on the surface chemistry and electronic properties of the catalyst [42].

To confirm the main active species and the potential reaction mechanism for superior photodegradability of the ZnFe-LDH photocatalyst, a trapping experiment was carried out without the electron acceptor added. In this study, IPA, EDTA, and AA were added to the reaction solutions as  $OH^\bullet$ ,  $h^+$ , and  $O_2^{\bullet-}$  scavengers, respectively [43,44]. The results are illustrated in Fig. 9. When the different scavengers are participated in the photocatalytic reaction, the RhB degradation performance is obviously reduced. The calculated RhB dye degradation efficiency of 23.12%, 19.37%, and 62.85% correspond to the scavengers IPA, EDTA, and AA, respectively. EDTA and IPA scavenger observed a major decline in the degradation efficiency, which inferred that  $h^+$  and  $OH^\bullet$  play a key role in the photocatalytic process. Based on this experiment, the role of active species in the photocatalytic degradation follows the order as  $h^+ > OH^\bullet > O_2^{\bullet-}$ .

Fig. 10 shows the degradation efficiency of the ZnFe-LDH100 samples for the different concentrations of H<sub>2</sub>O<sub>2</sub>. For the UV light-induced degradation, percentages in the

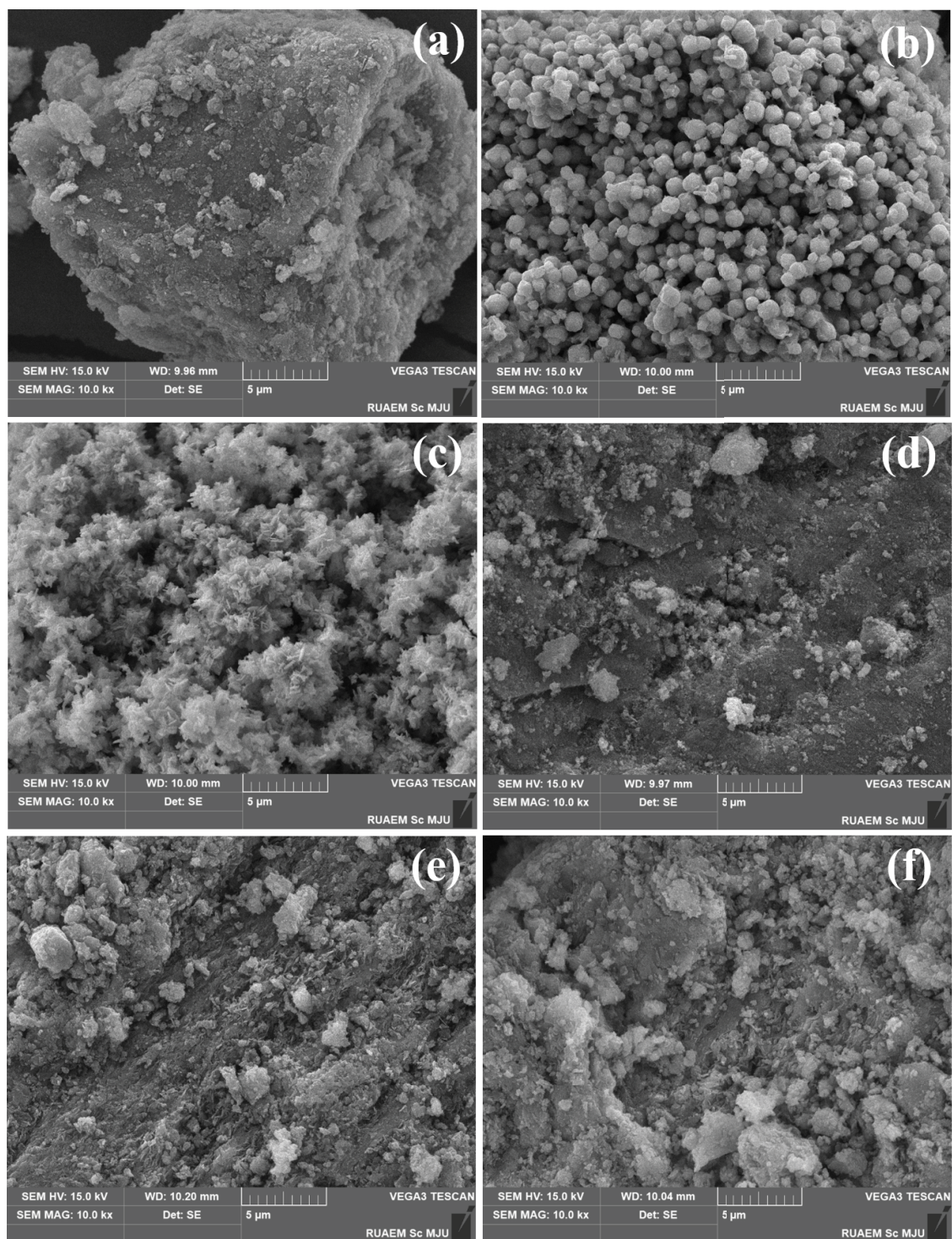


Fig. 5. Scanning electron micrograph of (a) iron ore (b)  $\text{Fe}_2\text{O}_3$ , (c)  $\text{ZnO}$ , (d)  $\text{ZnFe-LDH80}$ , (e)  $\text{ZnFe-LDH90}$ , and (f)  $\text{ZnFe-LDH100}$ .

range of 68.53%–100.00% with a kinetic rate constant in the range of 0.0348–0.2060  $\text{min}^{-1}$  were observed for  $\text{H}_2\text{O}_2$  concentrations of 0.0%–0.9% (Table 1). The highest efficiency was that for added 0.9% v/v  $\text{H}_2\text{O}_2$  with complete photodegradation in 20 min. The  $\text{H}_2\text{O}_2$  acted as an electron acceptor that prevented  $e^-/h^+$  pairs recombination as it trapped

photo-generated electrons and increased the availability of holes in the generation of reactive oxygen species (ROS) [45]. However, the addition of  $\text{H}_2\text{O}_2$  to the photocatalytic reaction could enhance the degradation efficiency by reacting with an electron to produce ROS as well. This might have been partly due to the presence of Fe in the  $\text{ZnFe-LDH}$  sample, which

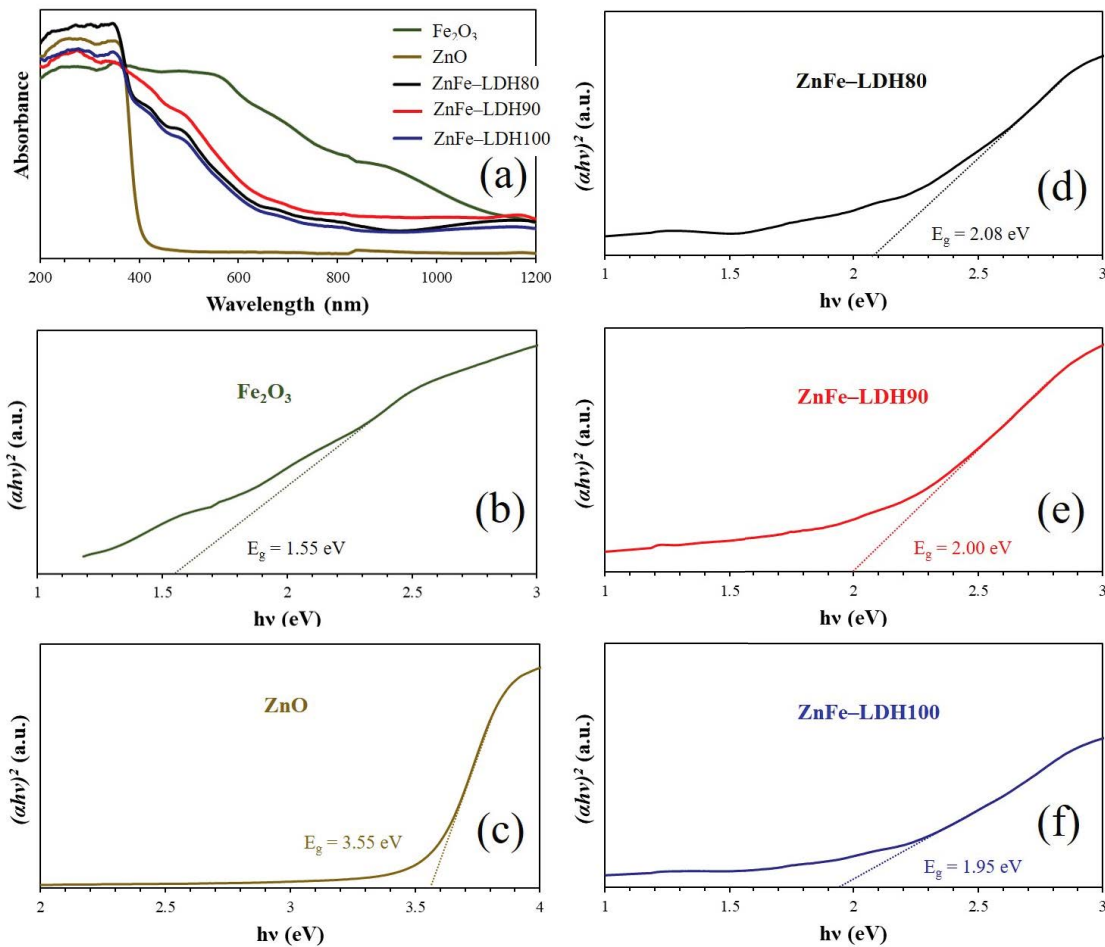


Fig. 6. UV-Vis optical analysis of prepared samples, (a) absorption spectra and plots of  $(\alpha h\nu)^2$  vs. photon energy ( $h\nu$ ) of (b)  $\text{Fe}_2\text{O}_3$ , (c)  $\text{ZnO}$ , (d)  $\text{ZnFe-LDH80}$ , (e)  $\text{ZnFe-LDH90}$ , and (f)  $\text{ZnFe-LDH100}$ .

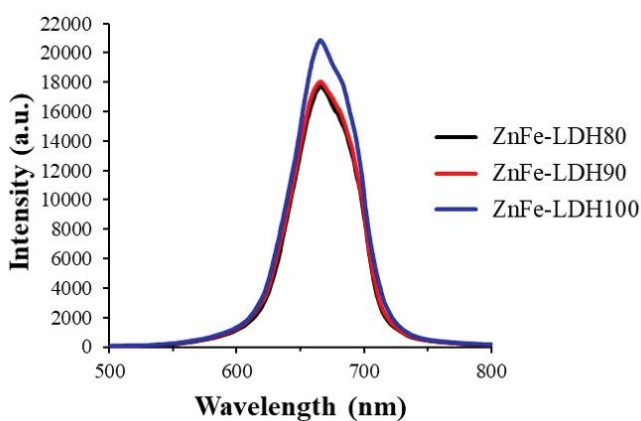


Fig. 7. Photoluminescence spectra of  $\text{ZnFe-LDH}$  nanostructures prepared with the hydrothermal method at  $80^\circ\text{C}$ – $100^\circ\text{C}$ .

could react with  $\text{H}_2\text{O}_2$  to produce more hydroxyl radicals and exhibit better photocatalytic activity [13].

Energy consumption is one of the various factors that can affect the selection of photocatalytic processes since it

affects the cost-effectiveness of the process. The electrical energy per order ( $E_{\text{EO}}$ ) was the parameter introduced in this research to evaluate advanced oxidation processes (photocatalytic process with UV).  $E_{\text{EO}}$  has been proposed as an indicator of process efficiency in terms of cost per unit volume for UV reactors. The following equation was used to calculate the  $E_{\text{EO}}$  values in  $\text{kWh/m}^3$  order given the first-order degradation reaction [46,47]:

$$E_{\text{EO}} = \frac{(38.4 \times P)}{(V \times K)} \quad (5)$$

where  $P$  is the power of the light source (kW) and  $V$  is the solution volume (L). As displayed in Table 1, the calculated  $E_{\text{EO}}$  values ranged from 264.82 to 708.92  $\text{kWh/m}^3$  for the case without an electron acceptor. In terms of the energy consumption in the photocatalytic degradation process, it was found that more than two times the energy was to be able to be saved when  $\text{ZnFe-LDH100}$  was used as a photocatalyst compared to photolysis. For the case of an electron acceptor being added, the calculated  $E_{\text{EO}}$  was in the range of 44.74–264.83  $\text{kWh/m}^3$ , which was found to decrease as the

concentration of the  $H_2O_2$  electron acceptor in the photocatalytic reaction increased. Based on the experimental results, the energy consumption could be reduced by approximately six times when the  $H_2O_2$  electron acceptor concentration was increased from 0.0% to 0.9%. The addition of an electron acceptor could reduce the energy consumption of the photocatalytic processes. This was consistent with the previous report of Elbadawy et al. [48]. It was found that the addition of the electron acceptor reduced the energy consumption from 714.29 to 117.6 kWh in the UV/TiO<sub>2</sub>/ZnO/H<sub>2</sub>O<sub>2</sub> system at pH = 6.5. Energy consumption is a cost-effective indicator for a photocatalytic process that depends on the kinetic rate of the reaction.  $E_{EO}$  is considered a key factor in the selection of photocatalytic processes, but there have been no previously reported studies on the energy consumption of ZnFe-LDH photocatalysts.

Fig. 11 shows the five cycles of reusability tested with the photocatalytic degradation of RhB under UV light. A

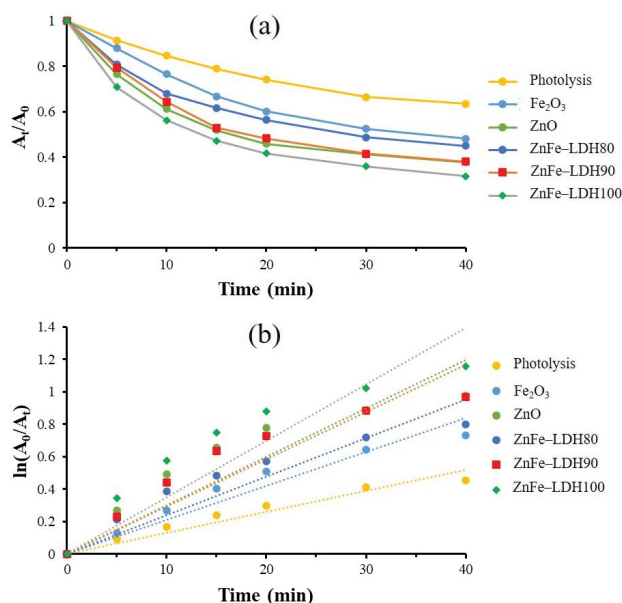


Fig. 8. The photocatalyst comparisons of the samples prepared with the hydrothermal method, (a) degradation efficiency and (b) pseudo-first-order kinetic plot.

Table 1  
Photocatalytic efficiency, kinetic rate constant, and  $E_{EO}$  values of the samples

Samples	Efficiency (%)	$K$ (min <sup>-1</sup> )	$R^2$	$E_{EO}$ (kWh/m <sup>3</sup> )
Photolysis	36.53	0.0130	0.9818	708.92
Fe <sub>2</sub> O <sub>3</sub>	51.91	0.0210	0.9712	438.85
ZnO	62.35	0.0238	0.9585	387.22
ZnFe-LDH80	55.12	0.0292	0.9554	315.61
ZnFe-LDH90	62.06	0.0300	0.9465	307.20
ZnFe-LDH100	68.53	0.0348	0.9465	264.82
ZnFe-LDH100 + 0.3% $H_2O_2$	71.00	0.0373	0.9459	247.08
ZnFe-LDH100 + 0.6% $H_2O_2$	100.00	0.0940	0.9961	98.04
ZnFe-LDH100 + 0.9% $H_2O_2$	100.00	0.2060	0.9993	44.74

total of five test cycles showed the degradation efficiency for each cycle, as follows. The first two cycles could be completely degraded in 20 and 40 min. The efficiencies of the last three cycles were decreased by 4.17%, 8.33%, and 12.50%. The results revealed that the efficiency exhibited a 12.5% decrease in the total efficiency after five cycles were run, which could have resulted from the photo-corrosion phenomenon [49]. The ZnFe-LDH photocatalyst prepared from low-cost natural iron ore was reasonably stable.

According to the experimental results, a possible mechanism for the photocatalytic degradation of RhB using ZnFe-LDH under UV light irradiation was proposed as shown in Fig. 12.

The primary mechanism for the photocatalytic degradation of the RhB solution is presented below [20,50]. The ZnFe-LDH photocatalysts could be irradiated with light with energy greater than their bandgap, thus producing ZnFe-LDH ( $e_{CB}^- + h_{VB}^+$ ) pairs in the conduction and valence bands [Eq. (6)].



The ZnFe-LDH ( $h_{VB}^+$ ) was oxidized with  $H_2O$ , yielding  $OH^\bullet$ , as shown in Eqs. (7) and (8), while the ZnFe-LDH ( $e_{CB}^-$ ) reacted with  $O_2$  to produce  $O_2^{\bullet-}$ , as illustrated in Eq. (9).

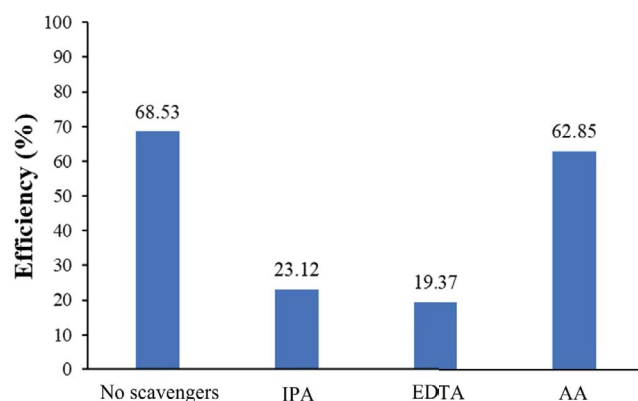
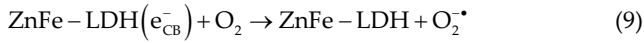
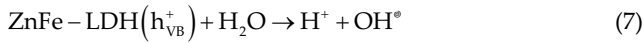
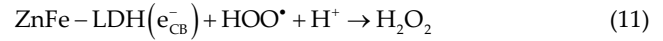


Fig. 9. Active species trapping experiment over ZnFe-LDH100 photocatalyst.



Additionally, the  $\text{O}_2^{\bullet-}$  could react with  $\text{H}^+$  and ZnFe-LDH ( $e_{\text{CB}}^-$ ) to produce  $\text{OH}^\bullet$ , as shown in Eqs. (10)–(12). The  $\text{H}_2\text{O}_2$  added to the photocatalytic reaction could react according to Eqs. (12) and (13), reducing the recombination rate and increasing the ROS yield.



All of the  $\text{OH}^\bullet$ ,  $\text{O}_2^{\bullet-}$ , and  $\text{H}_2\text{O}_2$  formed in the photocatalytic reaction resulted in RhB degradation [Eqs. (14) and (15)]. The degradation of RhB involves a de-ethylation

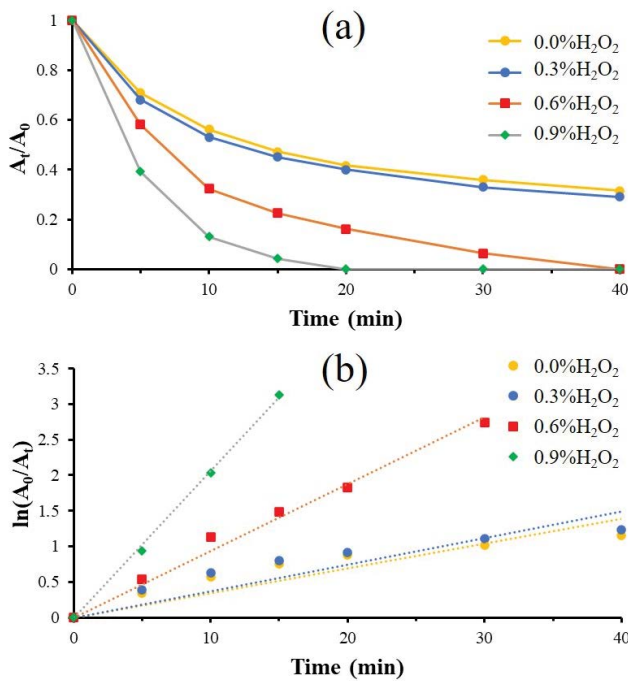


Fig. 10. Effects of the different concentrations of the electron acceptor on the photocatalytic degradation of Rhodamine B under UV light irradiation.

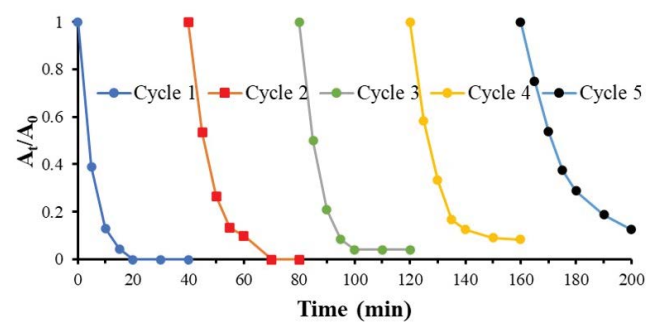


Fig. 11. Five cycle reusability test of ZnFe-LDH100 on the photocatalytic degradation of Rhodamine B under UV light irradiation.

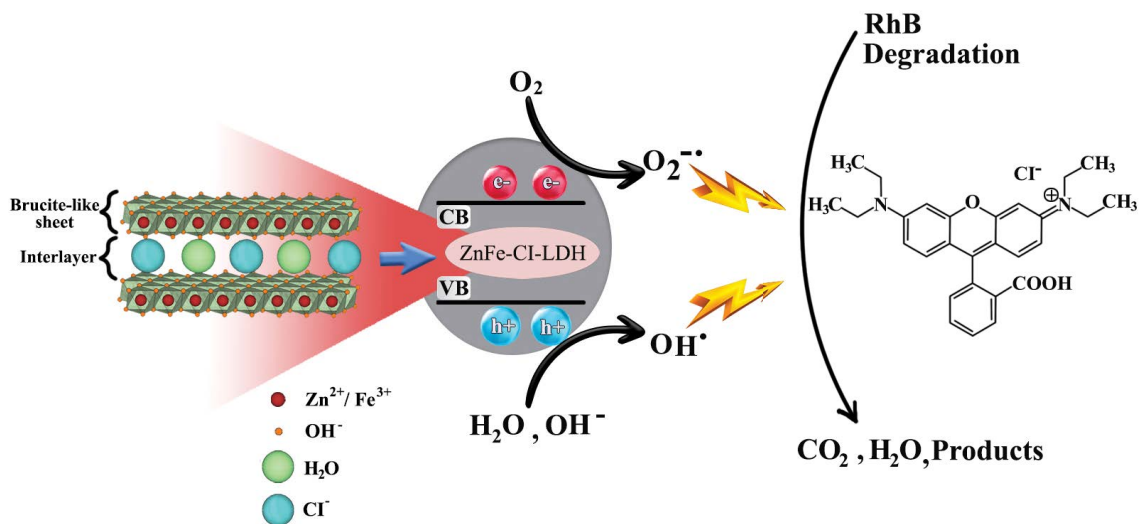
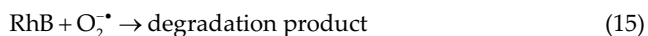
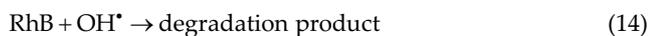


Fig. 12. Schematic illustration of the mechanism for photocatalytic degradation of Rhodamine B by ZnFe-LDH.

process. It has been observed that each de-ethylated step results in a blue shift of the maximum absorption band [51].



Based on this work, there are several benefits in using ZnFe-LDH in photocatalysis. First, the preparation process can save energy by using a temperature below that used for the preparation of mixed metal oxides without a calcination process [52]. Second, the photocatalyst is inexpensive because it uses a precursor made from natural iron ore. Finally, it possesses good photocatalytic properties, including high crystallinity, small crystals, and uniform particles, and good optical properties. In addition, the performance of a ZnFe-LDH photocatalyst can also be enhanced with composites with other agents such as polypyrrole nanofiber [53], diatomite [54], and  $(\text{BiO})_2\text{CO}_3$  [55], etc. The  $E_{\text{EO}}$  is a value indicating the amount of electricity used in a photocatalytic process to remove at least 90% of the pollutants. This means that the process is highly efficient when the pollutant concentrations are low. These allow cost estimates and are used to make investment decisions in the treatment system [56].

#### 4. Conclusions

In this work, low-cost iron ore from natural sources was utilized in the preparation of ZnFe-LDH nanostructures for use in photocatalytic degradation of RhB. The main focus of this study was to prove the feasibility, efficacy, and cost-effectiveness of natural iron ore for use in advanced oxidation photocatalysis. ZnFe-LDH nanostructures were prepared with the low-temperature hydrothermal method. The optimum condition for the preparation of ZnFe-LDH nanostructures was 100°C for 36 h. The prepared nanostructures had good photocatalyst properties such as high crystallinity, small crystallite size, particle uniformity, and narrow band-gap energy. For the photocatalytic process, the experimental finding indicated that the UV/ZnFe-LDH/ $\text{H}_2\text{O}_2$  process was the most energy-efficient system for RhB degradation. The system was also found to be highly stable, with only a 12.5% reduction in efficiency after five cycles were run. The photodegradation process was found to have energy savings of more than 15 times and 2 times for photocatalysis with and without the additions of 0.9%  $\text{H}_2\text{O}_2$ , respectively, compared to photolysis. Moreover, experiments were conducted to demonstrate that ZnFe-LDH was particularly suitable for the photocatalytic degradation of environmental pollutants in terms of low-cost photocatalysts and energy savings in the photocatalytic process. Based on the research results, they could be confirmed that this approach increases the value of natural low-cost materials in a simple and effective process. This could also be extended to large-scale production.

#### Conflicts of interest

The authors declare that there are no conflicts of interest regarding the publication of this paper.

#### Acknowledgements

This work was supported by the Thailand Science Research and Innovation (TSRI), whom the authors thank for their financial support. The authors also acknowledge the energy and environment research centre, Uttaradit Rajabhat University, Uttaradit, Thailand for the use of their research equipment.

#### References

- [1] L. Wang, Z. Zhu, F. Wang, Y. Qi, W. Zhang, C. Wang, State-of-the-art and prospects of Zn-containing layered double hydroxides (Zn-LDH)-based materials for photocatalytic water remediation, *Chemosphere*, 278 (2021) 130367, doi: 10.1016/j.chemosphere.2021.130367.
- [2] M. El Alouani, S. Alehyen, H. El Hadki, H. Saufi, A. Elhalil, O.K. Kabbaj, M. Taibi, Synergetic influence between adsorption and photodegradation of Rhodamine B using synthesized fly ash based inorganic polymer, *Surf. Interfaces*, 24 (2021) 101136, doi: 10.1016/j.surfin.2021.101136.
- [3] M. Hassanpour, H. Safardoust-Hojaghan, M. Salavati-Niasari, Degradation of methylene blue and Rhodamine B as water pollutants via green synthesized  $\text{Co}_3\text{O}_4/\text{ZnO}$  nanocomposite, *J. Mol. Liq.*, 229 (2017) 293–299.
- [4] S. Zinatloo-Ajabshir, M.S. Morassaei, M. Salavati-Niasari, Facile fabrication of  $\text{Dy}_2\text{Sn}_2\text{O}_7\text{-SnO}_2$  nanocomposites as an effective photocatalyst for degradation and removal of organic contaminants, *J. Colloid Interface Sci.*, 497 (2017) 298–308.
- [5] A. Elhalil, W. Boumya, A. Machrouhi, R. Elmoubarki, S. Mansouri, M. Sadiq, M. Abdennouri, N. Barka, Synthesis, characterization and efficient photocatalytic properties of spinel materials for dye degradation, *Appl. Surf. Sci. Adv.*, 13 (2023) 100381, doi: 10.1016/j.apsadv.2023.100381.
- [6] F.Z. Janani, N. Taoufik, H. Khiar, W. Boumya, A. Elhalil, M. Sadiq, A.V. Puga, N. Barka, Nanostructured layered double hydroxides based photocatalysts: insight on synthesis methods, application in water decontamination/splitting and antibacterial activity, *Surf. Interfaces*, 25 (2021) 101263, doi: 10.1016/j.surfin.2021.101263.
- [7] Z.-Z. Yang, C. Zhang, G.-M. Zeng, X.-F. Tan, D.-L. Huang, J.-W. Zhou, Q.-Z. Fang, K.-H. Yang, H. Wang, J. Wei, K. Nie, State-of-the-art progress in the rational design of layered double hydroxide based photocatalysts for photocatalytic and photoelectrochemical  $\text{H}_2/\text{O}_2$  production, *Coord. Chem. Rev.*, 446 (2021) 214103, doi: 10.1016/j.ccr.2021.214103.
- [8] S. Zinatloo-Ajabshira, M.S. Morassaeib, O. Amiric, M. Salavati-Niasari, Green synthesis of dysprosium stannate nanoparticles using *Ficus carica* extract as photocatalyst for the degradation of organic pollutants under visible irradiation, *Ceram. Int.*, 46 (2020) 6095–6107.
- [9] T. Dhanasekaran, A. Padmanaban, G. Gnanamoorthy, S.P. kumar, S. Munusamy, A. Stephen, V. Narayanan, Preparation, characterization and enhanced photocatalytic degradation of organic pollutants using layered double hydroxides, *Mater. Today Proc.*, 5 (2018) 8981–8985.
- [10] G. Zhao, J. Zou, X. Chen, J. Yu, F. Jiao, Layered double hydroxides materials for photo(electro-) catalytic applications, *Chem. Eng. J.*, 397 (2020) 125407, doi: 10.1016/j.cej.2020.125407.
- [11] H. Boumeriame, E.S. Da Silva, A.S. Cherevan, T. Chafik, J.L. Faria, D. Eder, Layered double hydroxide (LDH)-based materials: a mini-review on strategies to improve the performance for photocatalytic water splitting, *J. Energy Chem.*, 64 (2022) 406–431.
- [12] D.-G. Jeung, H.-J. Kim, J.-M. Oh, Incorporation of *Glycine max Merrill* extract into layered double hydroxide through ion-exchange and reconstruction, *Nanomaterials (Basel)*, 9 (2019) 1262, doi: 10.3390/nano9091262.
- [13] Z.-H. Xie, H.-Y. Zhou, C.-S. He, Z.-C. Pan, G. Yao, B. Lai, Synthesis, application and catalytic performance of layered double hydroxide based catalysts in advanced oxidation processes for wastewater decontamination: a review, *Chem. Eng. Sci.*, 414 (2021) 128713, doi: 10.1016/j.ces.2021.128713

- [14] Z. Dong, Y. Wu, Magnetically separable photocatalyst of direct Z-scheme  $g\text{-C}_3\text{N}_4$  nanosheets/natural hematite ore hybrids, *J. Photochem. Photobiol., A*, 336 (2017) 156–163.
- [15] A. Noruozi, A. Nezamzadeh-Ejhi, Preparation, characterization, and investigation of the catalytic property of  $\alpha\text{-Fe}_2\text{O}_3\text{-ZnO}$  nanoparticles in the photodegradation and mineralization of methylene blue, *Chem. Phys. Lett.*, 752 (2020) 137587, doi: 10.1016/j.cplett.2020.137587.
- [16] Y. Wu, L. Liu, X. Yu, J. Zhang, L. Li, C. Yan, B. Zhu, Natural hematite ore composited with ZnO nanoneedles for energy applications, *Composites, Part B*, 137 (2018) 178–183.
- [17] S. Sharma, G. Sharma, A. Kumar, P. Dhiman, T.S. AlGarni, M. Naushad, Z.A.A. Othman, F.J. Stadler, Controlled synthesis of porous Zn/Fe based layered double hydroxides: synthesis mechanism, and ciprofloxacin adsorption, *Sep. Purif. Technol.*, 278 (2022) 119481, doi: 10.1016/j.seppur.2021.119481.
- [18] E.M. Seftel, P. Cool, D. Lutić, Mg-Al and Zn-Fe layered double hydroxides used for organic species storage and controlled release, *Mater. Sci. Eng., C*, 33 (2013) 5071–5078.
- [19] K.M. Parida, L. Mohapatra, Carbonate intercalated Zn/Fe layered double hydroxide: a novel photocatalyst for the enhanced photo degradation of azo dyes, *Chem. Eng. J.*, 179 (2012) 131–139.
- [20] N. Gu, J. Gao, K. Wang, B. Li, W. Dong, Y. Ma, *Microcystis aeruginosa* inhibition by Zn-Fe-LDHs as photocatalyst under visible light, *J. Taiwan Inst. Chem. Eng.*, 64 (2016) 189–195.
- [21] P.Y. Motlagh, A. Khataee, T.S. Rad, A. Hassani, S.W. Joo, Fabrication of ZnFe-layered double hydroxides with graphene oxide for efficient visible light photocatalytic performance, *J. Taiwan Inst. Chem. Eng.*, 101 (2019) 186–203.
- [22] N.K. Gupta, M. Saifuddin, S. Kim, K.S. Kim, Microscopic, spectroscopic, and experimental approach towards understanding the phosphate adsorption onto Zn-Fe layered double hydroxide, *J. Mol. Liq.*, 297 (2020) 111935, doi: 10.1016/j.molliq.2019.111935.
- [23] F. Liu, X. Liang, S. He, F. Li, Y. Jin, Z. Zhao, L. Zhu, Performance of a new low-cost Zn/Fe-layered double hydroxide-modified ceramsite for the removal of P from agricultural runoff, *Ecol. Eng.*, 159 (2021) 106117, doi: 10.1016/j.ecoleng.2020.106117.
- [24] S.A.A. Moaty, A.A. Farghali, R. Khaled, Preparation, characterization and antimicrobial applications of Zn-Fe LDH against MRSA, *Mater. Sci. Eng., C*, 68 (2016) 184–193.
- [25] S. Zinatloo-Ajabshira, S. Mortazavi-Derazkolab, M. Salavati-Niasari,  $\text{Nd}_2\text{O}_3\text{-SiO}_2$  nanocomposites: a simple sonochemical preparation, characterization and photocatalytic activity, *Ultrason. Sonochem.*, 42 (2018) 171–182.
- [26] S. Chang, X. Wang, Q. Hu, X. Sun, A. Wang, X. Dong, Y. Zhang, L. Shi, Q. Sun, Self-assembled nanocomposites and nanostructures for environmental and energy applications, *Crystals*, 12 (2022) 274, doi: 10.3390/cryst12020274.
- [27] P. Jansanthea, C. Saovakon, W. Chomkitichai, J. Ketwaraporn, S. Maneepong, N. Chaiwong, K. Jaisee, C. Wansao, A. Wanaek, P. Pookmanee, Thiamethoxam insecticide degradation with a leaf-like cupric oxide monoclinic structure synthesized via the microwave method, *Russ. J. Inorg. Chem.*, 66 (2021) 667–678.
- [28] P. Jansanthea, J. Kanthabangharn, W. Chomkitichai, J. Ketwaraporn, C. Saovakon, C. Wansao, A. Wanaek, P. Kraivuttinun, P. Pookmanee, S. Phanichphant, Temperature-controlled synthesis and photocatalytic properties of ZnO-SnO<sub>2</sub> nanocomposites, *J. Aust. Ceram. Soc.*, 57 (2021) 579–588.
- [29] A.M.G. Domacena, C.L.E. Aquino, M.D.L. Balela, Photo-Fenton degradation of methyl orange using hematite ( $\alpha\text{-Fe}_2\text{O}_3$ ) of various morphologies, *Mater. Today Proc.*, 22 (2020) 248–254.
- [30] A.A.A. Ahmed, Z.A. Talib, M.Z. Hussein, M.H. Flaifel, N.M. Al-Hada, Influence of Zn/Fe molar ratio on optical and magnetic properties of ZnO and ZnFe<sub>2</sub>O<sub>4</sub> nanocrystal as calcined products of layered double hydroxides, *J. Spectrosc.*, 2014 (2014) 1–6.
- [31] K. Nejati, A.R. Akbari, S. Davari, K. Asadpour-Zeynali, Z. Rezvani, Zn-Fe-layered double hydroxide intercalated with vanadate and molybdate anions for electrocatalytic water oxidation, *New J. Chem.*, 42(4) (2018) 2889–2895.
- [32] M.A. Shehu, A.M. Bello, Zn/Fe-NO<sub>3</sub> layered double hydroxides: synthesis, characterization and photocatalytic activity on phenol red degradation, *Niger. Res. J. Chem. Sci.*, 9 (2021) 199–209.
- [33] M. Saeed, M. Zafar, A. Razaq, S.A. Khan, Z. Khan, W.Y. Kim, Visible-light-active Zn-Fe layered double hydroxide (LDH) for the photocatalytic conversion of rice husk extract to value-added products, *Appl. Sci.*, 12 (2022) 2313, doi: 10.3390/app12052313.
- [34] O. Koba-Ucun, T.Ö. Hanci, I. Arslan-Alaton, S. Arefi-Oskoui, A. Khataee, M. Kobya, Y. Orooji, Toxicity of Zn-Fe layered double hydroxide to different organisms in the aquatic environment, *Molecules*, 26 (2021) 395, doi: 10.3390/molecules26020395.
- [35] S. Bouteraa, S. Hamouda, N. Bettahar, Synthesis of Zn-Fe layered double hydroxides (LDH) by using Zn and Fe(II) salts and removal behavior research of anionic dye, RHAZES: *Green Appl. Chem.*, 15 (2022) 71–82.
- [36] M.T. Amin, A.A. Alazba, M. Shafiq, Synthesis and characterization of Zn/Fe layered double hydroxide and its composites for copper adsorption from aqueous solution, *Desal. Water Treat.*, 218 (2021) 281–293.
- [37] L. Wang, M. Zhang, B. Li, Thermal analysis and flame-retarded mechanism of composites composed of ethylene vinyl acetate and layered double hydroxides containing transition metals (Mn, Co, Cu, Zn), *Appl. Sci.*, 6 (2016) 131, doi: 10.3390/app6050131.
- [38] L. Vigna, A. Nigro, A. Verna, I.V. Ferrari, S.L. Marasso, S. Bocchini, M. Fontana, A. Chiodoni, C.F. Pirri, M. Cocuzza, Layered double hydroxide-based gas sensors for VOC detection at room temperature, *ACS Omega*, 6 (2021) 20205–20217.
- [39] W. Liang, I. Zhitomirsky, Zn-Fe double hydroxide-carbon nanotube anodes for asymmetric supercapacitors, *Front. Mater.*, 7 (2020) 1–8.
- [40] R.K. Mahmoud, M. Taha, A. Zaher, R.M. Amin, Understanding the physicochemical properties of Zn-Fe LDH nanostructure as sorbent material for removing of anionic and cationic dyes mixture, *Sci. Rep.*, 11 (2021) 21365, doi: 10.1038/s41598-021-00437-w.
- [41] R.G. Ciocarlan, H. Wang, B. Cuypers, M. Mertens, Y. Wu, S.V. Doorslaer, E.M. Seftel, P. Cool, ZnTi layered double hydroxides as photocatalysts for salicylic acid degradation under visible light irradiation, *Appl. Clay Sci.*, 197 (2020) 105757, doi: 10.1016/j.clay.2020.105757.
- [42] G. Zhang, X. Zhang, Y. Meng, G. Pan, Z. Ni, S. Xia, Layered double hydroxides-based photocatalysts and visible-light-driven photodegradation of organic pollutants: a review, *Chem. Eng. J.*, 392 (2020) 123684, doi: 10.1016/j.cej.2019.123684.
- [43] H.A. Ahsaine, A.E. Jaouhari, A. Slassi, M. Ezahri, A. Benlhachemi, B. Bakiz, F. Guinneton, J.-R. Gavari, Electronic band structure and visible-light photocatalytic activity of Bi<sub>2</sub>WO<sub>6</sub>: elucidating the effect of lutetium doping, *RSC Adv.*, 6 (2016) 101105–101114.
- [44] Y. Naciri, H.A. Ahsaine, A. Chennah, A. Amedlous, A. Taoufyq, B. Bakiz, M. Ezahri, S. Villain, A. Benlhachemi, Facile synthesis, characterization and photocatalytic performance of Zn<sub>3</sub>(PO<sub>4</sub>)<sub>2</sub> platelets toward photodegradation of Rhodamine B dye, *J. Environ. Chem. Eng.*, 6 (2018) 1840–1847.
- [45] J.M. Monteagudo, A. Durán, I.S. Martín, B. Vellón, Photocatalytic degradation of aniline by solar/TiO<sub>2</sub> system in the presence of the electron acceptors Na<sub>2</sub>S<sub>2</sub>O<sub>8</sub> and H<sub>2</sub>O<sub>2</sub>, *Sep. Purif. Technol.*, 238 (2020) 116456, doi: 10.1016/j.seppur.2019.116456.
- [46] O. Keen, J. Bolton, M. Litter, K. Bircher, T. Oppenländer, Standard reporting of electrical energy per order ( $E_{EO}$ ) for UV/H<sub>2</sub>O<sub>2</sub> reactors (IUPAC Technical Report), *Pure Appl. Chem.*, 90 (2018) 1487–1499.
- [47] F. Barjasteh-Askari, S. Nasserri, R. Nabizadeh, A. Najafpoor, M. Davoudi, A.-H. Mahvi, Photocatalytic removal of diazinon from aqueous solutions: a quantitative systematic review, *Environ. Sci. Pollut. Res. Int.*, 29 (2022) 26113–26130.
- [48] H.A. Elbadawy, W.A. Sadik, A.F. Elhusseiny, S.M. Hussein, Design of economic photocatalytic system with low energy consumption, and high quantum yield, for the degradation of

- Acid Red 37 textile dye, *Process Saf. Environ. Prot.*, 148 (2021) 1191–1206.
- [49] M. Sarafraz, M. Sadeghi, A. Yazdanbakhsh, M.M. Amini, M. Sadani, A. Eslami, Enhanced photocatalytic degradation of ciprofloxacin by black Ti<sup>3+</sup>/N-TiO<sub>2</sub> under visible LED light irradiation: kinetic, energy consumption, degradation pathway, and toxicity assessment, *Process Saf. Environ. Prot.*, 137 (2020) 261–272.
- [50] M. Kurian, Advanced oxidation processes and nanomaterials – a review, *Cleaner Eng. Technol.*, 2 (2021) 100090, doi: 10.1016/j.clet.2021.100090.
- [51] H. Ait Ahsaine, M. Ezahri, A. Benlhachemi, B. Bakiz, S. Villain, F. Guinneton, J.-R. Gavarri, Novel Lu-doped Bi<sub>2</sub>WO<sub>6</sub> nanosheets: synthesis, growth mechanisms and enhanced photocatalytic activity under UV-light irradiation, *Ceram. Int.*, 42 (2016) 8552–8558.
- [52] T. Taher, N.R. Palapa, R. Mohadi, A. Lesbani, Thermal reconstruction properties of ZnFe LDH prepared by facile hydrothermal route, *AIP Conf. Proc.*, 2242 (2020) 040058–1–040058–5, doi: 10.1063/5.0007984.
- [53] F. Mohamed, M.R. Abukhadra, M. Shaban, Removal of safranin dye from water using polypyrrole nanofiber/Zn-Fe layered double hydroxide nanocomposite (Ppy NF/Zn-Fe LDH) of enhanced adsorption and photocatalytic properties, *Sci. Total Environ.*, 640–641 (2018) 352–363.
- [54] G. Zhao, L. Liu, C. Li, T. Zhang, T. Yan, J. Yu, X. Jiang, F. Jiao, Construction of diatomite/ZnFe layered double hydroxides hybrid composites for enhanced photocatalytic degradation of organic pollutants, *J. Photochem. Photobiol., A*, 367 (2018) 302–311.
- [55] Y. Wang, L. Wang, Z. Xiao, S. Liu, J. Hu, X. Long, L. Wu, C. Sun, K. Chen, F. Jiao, Construction of Z-scheme heterojunction of (BiO)<sub>2</sub>CO<sub>3</sub>/ZnFe-LDH for enhanced photocatalytic degradation of tetracycline, *J. Alloys Compd.*, 900 (2022) 163450, doi: 10.1016/j.jallcom.2021.163450.
- [56] K. Zatloukalová, L. Obalová, K. Kočí, L. Čapek, Z. Matěj, H. Šnajdhaufová, J. Ryczkowski, G. Słowik, Photocatalytic degradation of endocrine disruptor compounds in water over immobilized TiO<sub>2</sub> photocatalysts, *Iran. J. Chem. Chem. Eng.*, 36 (2017) 29–38.